Exemption of Lattice Collapse in Ni–MnO2 Birnessite Regulated by the Structural Water Mobility

Journal:	*Journal of Materials Chemistry A*
Manuscript ID	TA-COM-08-2021-006716.R2
Article Type:	Communication
Date Submitted by the Author:	28-Sep-2021
Complete List of Authors:	Teng, Xiaowei; University of New Hampshire, Chemical Engineering Shan, Xiaoqiang; University of New Hampshire, Chemical Engineering Pidathala, Ranga ; University of Louisville, Department of Mechanical Engineering Kim, SaeWon; University of New Hampshire, Chemical Engineering Xu, Wenqian; Argonne National Laboratory, X-ray Science Division, Advanced Photon Source Abeykoon, Milinda; Brookhaven National Laboratory, Photon Science Division - National Synchrotron Light Source II Kwon, Gihan; Brookhaven National Laboratory, Photon Science Division - National Synchrotron Light Source II Olds, Daniel; Brookhaven National Laboratory, Photon Science Division - National Synchrotron Light Source II Narayanan, Badri; Argonne National laboratory, Materials Science Division; University of Louisville, Department of Mechanical Engineering

COMMUNICATION

Exemption of Lattice Collapse in Ni-MnO$_2$ Birnessite Regulated by the Structural Water Mobility

Xiaoqiang Shan,[a] Ranga Teja Pidathala, [b] SaeWon Kim,[a] Wenqian Xu,[c] Milinda Abeykoon,[d] Gihan Kwon,[d] Daniel Olds,[d] Badri Narayanan,[b] and Xiaowei Teng*[a]

Lattice collapse and associated mechanical fracture frequently occur in Li-intercalated metal oxide cathodes at the deep charge upon Li-ion removal, governed by chemical compositions and the resulting electron density of the oxygen atoms.   However, similar lattice collapse for metal oxide electrodes in aqueous storage and its mitigation have not been well studied. Herein, we reported the lattice collapse of MnO$_2$ layered birnessite during the aqueous de-sodiation process at high voltage due to the structural water motion, evidenced by *in situ* XRD.   Unlike non-aqueous Li-intercalated electrodes, Ni-dopants mitigated the lattice collapse of birnessite at deep charge states. Moreover, density functional theory (DFT) calculations showed that Ni doping induces charge depletion of lattice oxygen due to its higher electronegativity than Mn. This charge reduction, in turn, yields a significant decrease in electrostatic repulsion between the oxygens belonging to lattice and structural water. Classical molecular dynamics simulations based on atomic charges obtained from DFT elucidate that Ni-doping facilitates immobilization of structural water in (Ni)MnO$_2$ and prevents lattice collapse upon Na-ion removal. (Ni)MnO$_2$ exempted from lattice collapse shows an improved storage capacity relative to MnO$_2$ while maintaining similar cycling stability.

Introduction

Layered transition metal oxides (TMOs) are attractive high-capacity electrode materials for electrochemical energy storage owing to their large interlayer spacing, i.e., the distance between the adjacent transition metal-oxygen polyhedral layers, where the alkali ions are accommodated.[1, 2] Ni-rich LiNi$_{1-x-y}$Co$_x$Mn$_y$O$_2$ (NCM) is a promising layered cathode material in non-aqueous Li-ion batteries. But it suffers from significant capacity fading and low structural stability at high voltages, limiting its stable operation.[3] The negative charge transfer from O to Ni atoms in highly charged NCM depletes the effective oxygen charge, reduces repulsion between Li-metal-O polyhedral slabs, and causes an abrupt collapse of the interlayer spacing (*c*-lattice).[4, 5] Recent results showed that charge-transfer-induced lattice collapse in NCM materials on the deep charge states is instead a universal behavior unaffected by Co or Mn substitution.[6-8] Such anisotropic lattice changes during Li-removal (charging) cause mechanical strain at the grain boundaries, causing the fracture of the primary electrode material and mechanical disintegration.[1] The abrupt collapse of the *c*-lattice at highly charged states was recently reported in aqueous layered Na$_x$MnO$_2$ birnessite electrode materials at high voltage.[9] Unlike non-aqueous NCM Li-ion electrode, MnO$_2$ birnessite possesses cations (e.g., Na$^+$) and water in the interlayers of [MnO$_6$] octahedral layers and the large interlayer spacing around 7 Å to accommodate Na-ions. In general, when MnO$_2$ birnessite experiences pseudocapacitive alkali ion storage with a relatively low storage capacity (< 40 mAh/g), its lattice structure with slight lattice changes upon charging and discharging process within a moderate voltage window (i.e., -0.05 V to 0.85 V vs. Ag/AgCl).[10] However, when MnO$_2$ birnessite experienced the deep charge at high voltage, the *c*-lattice collapse of 0.4 % was observed. As MnO$_2$ birnessite is one of the essential cathode materials for aqueous batteries, and thus, it is of great significance to understand and mitigate the lattice collapse in MnO$_2$ birnessite while sustaining storage capacity and structural stability.

Given the promise of TMO layered electrode materials for alkali ion storage in both aqueous and non-aqueous electrolytes, an essential question remains open on whether the lattice collapse could be effective*y* suppressed during the deep charge without compromising its storage capacity. Previous results showed that the lattice collapse of NCM

a. *Department of Chemical Engineering, University of New Hampshire, Durham, New Hampshire 03824, USA*

b. *Department of Mechanical Engineering, University of Louisville, Louisville, Kentucky 40292, USA*

c. *Advanced Photo Source, Argonne National Laboratory, Argonne, Illinois 60439, USA*

d. *National Synchrotron Light Source II, Brookhaven National Laboratory, Upton, New York 11973, USA*
E-mail: xw.teng@unh.edu
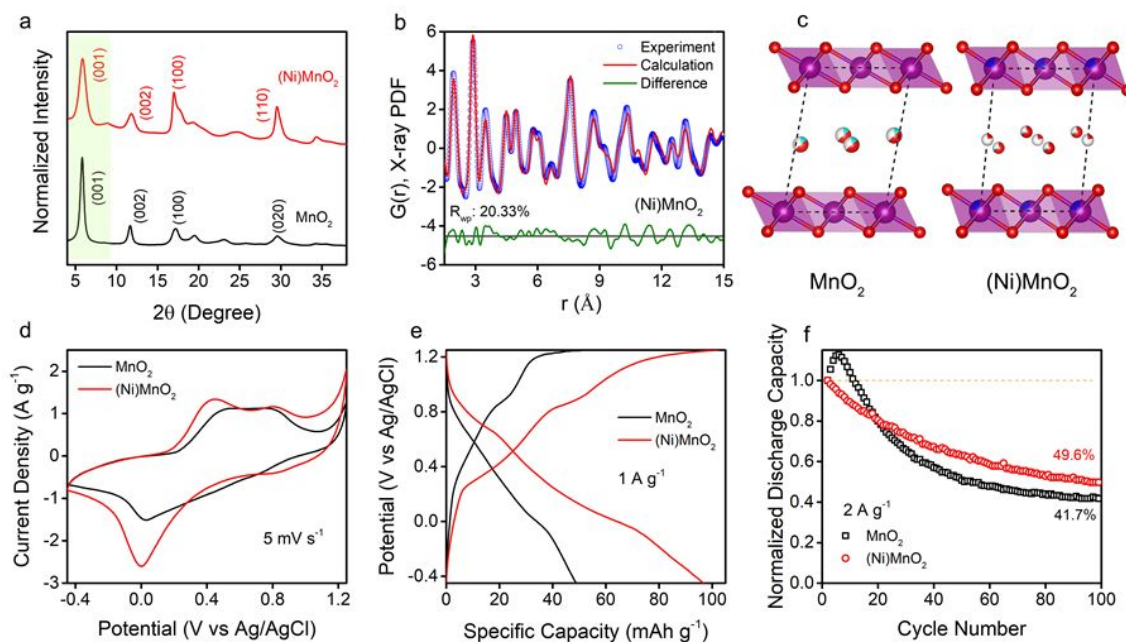
Figure 1. (a) XRD of layered MnO_2 and $(Ni)MnO_2$; (b) X-ray PDF analysis of $(Ni)MnO_2$; (c) crystal structures of MnO_2 and $(Ni)MnO_2$ with (001) layered planes (red: O; magenta: Mn; cyan: cations, e.g. Na-ion or K-ion; blue: Ni); (d) CV of MnO_2 and $(Ni)MnO_2$ from -0.45 to 1.25 V (vs Ag/AgCl) at the scan rate of 5 mV s^{-1}; (e) The CP of MnO_2 and $(Ni)MnO_2$ between -0.45 V and 1.25 V (vs Ag/AgCl) at current density of 1 A g^{-1}; (f) the normalized capacity retention at 2 A g^{-1} for 100 cycles.

materials could be mitigated by introducing alien ions (dopants) such as Al, Mg, and La, collectively.[8, 11-13] However, alleviation of lattice distortion always accompanies with a capacity penalty due to a less amount of Li extracted under the same electrochemical conditions. Here, we showed that Ni-doped birnessite [$(Ni)MnO_2$] instead exempted from lattice collapse due to the inhibited structural water motion during electrochemical cycling, different lattice variation mechanism observed in NCM materials. The density functional theory (DFT) calculations suggested that the decreased effective charge of oxygen atoms due to high-voltage Ni oxidation led to the decreased repulsion force between lattice oxygen and structural water oxygen, then lower mobility of structural water in $(Ni)MnO_2$ birnessite relative to MnO_2. Therefore, lattice collapse from co-de-intercalation and co-intercalation of structural water with Na-ions at the high voltage only occurs in MnO_2 while not for $(Ni)MnO_2$.

Results and discussion

MnO_2 and $Ni_{0.25}Mn_{0.75}O_2$ [$(Ni)MnO_2$] layered birnessite materials were synthesized using methods developed previously,[9, 14, 15] involving solid-state annealing of Mn_3O_4 with NaOH and co-precipitation of Mn and Ni salts in KOH solution. The synthesis details are provided in the experimental section. The chemical compositions of Na-intercalated MnO_2 and K-intercalated $(Ni)MnO_2$ birnessite were analyzed by Inductively Coupled Plasma-Mass Spectrometry (ICP-MS), showing formula of $Na_{0.27}MnO_2$ and $K_{0.12}(Ni_{0.23}Mn_{0.77})O_2$, respectively. Transmission electron microscopy (TEM) images show that MnO_2 and $(Ni)MnO_2$ birnessite have plate- or sheet-like two-dimensional morphologies (**Figure S1**). **Figure 1a** shows X-ray

diffraction (XRD) patterns of layered MnO_2 and $(Ni)MnO_2$m, confirming their birnessite-type MnO_2 layered structure comprised of [MnO_6] octahedral planes with structural water and cations (e.g., Na^+ or K^+) residing between interlayers.[9, 15] Both materials show the characteristic (001) basal diffraction peaks at low 2θ angles with d-spacing (d_{001}) of 7.1 Å for MnO_2 and 7.2 Å for $(Ni)MnO_2$, which could be attributed to several factors, such as structural water and alkali residing between interlayers, as well as the covalence of Mn-O and Ni-O bonds. Bragg diffraction peaks, including (100), (110), and (020), also appear at similar peak positions at higher 2θ angles. Notably, relative intensities of Bragg peaks to the (001) peak are different. Such peak broadening suggests the local structure of MnO_2 and $(Ni)MnO_2$ might be different. The diffraction has only involved the analysis of Bragg scattering, providing long-range ordering structure information. Thus, we conducted total X-ray scattering, including Bragg and diffuse scattering, and pair distribution function (PDF) analysis to comprehensively analyze the local structures of both materials, as shown in **Figures 1b and S2**. The resulting lattice parameters obtained from the PDF refinement are provided in **Tables S1 and S2**. PDF analysis suggested that both materials had a disordered long-range structure. However, in $(Ni)MnO_2$ octahedral layers, Ni-ions are homogeneously mixed into the [MnO_6] octahedral, while the Ni-site is relatively distorted compared to that of Mn (**Figure 1c**), confirmed by the larger ADP values of Ni sites relative to Mn sites (**Table S2**). Additionally, TGA measurements show similar water weight loss in MnO_2 (5.8%) and $(Ni)MnO_2$ (4.7%) (**Figure S3**), indicating the large amounts of structural water residing in the open space between interlayers. With similar crystal structures and morphologies, MnO_2 and $(Ni)MnO_2$ were then studied relatively to understand how Ni-dopant affects

COMMUNICATION
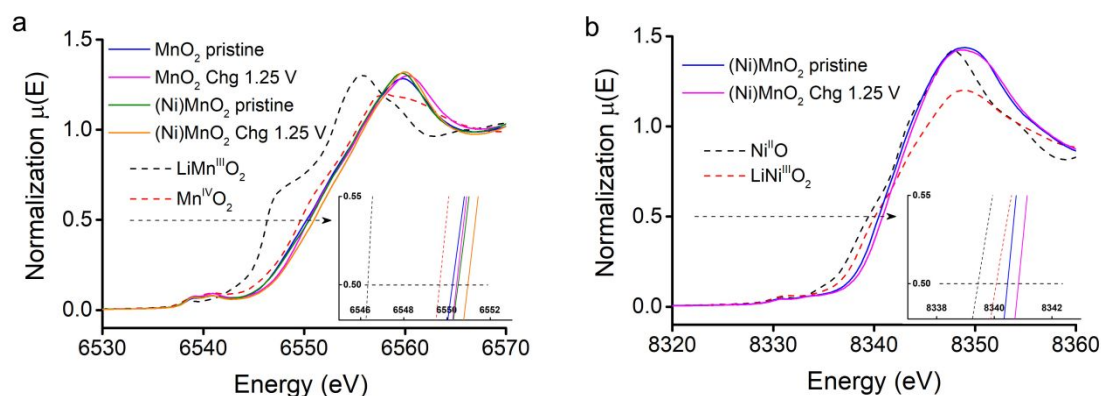
Figure 2. *Ex situ* XANES spectra of (a) Mn K-edge and (b) Ni K-edge for pristine and high-voltage charged MnO$_2$ and (Ni)MnO$_2$.

electrochemical charge-discharge behaviors as the cathodes for aqueous Na-ion storage. **Figure 1d** showed the cyclic voltammetry (CV) of MnO$_2$ and (Ni)MnO$_2$ conducted in three-electrode half-cells within 0.1M NaSO$_4$ solution at a scan rate of 5 mV s^{-1}. Notably, (Ni)MnO$_2$ showed a larger total charge storage capacitance than MnO$_2$ (489 coulomb g^{-1} vs. 367 coulomb g^{-1}), equivalent to the enclosed area from the CV for total charge storage. The results suggested Ni-doping improves the redox activity of MnO$_2$ materials, congruent with the fact that (Ni)MnO$_2$ showed more distinct redox peaks during the anodic and cathodic scans than MnO$_2$. **Figure 1e** shows the chronopotentiometry (CP) of MnO$_2$ and (Ni)MnO$_2$ conducted under the same conditions as CVs with two redox plateaus at charging and discharging profiles. (Ni)MnO$_2$ showed a higher discharge capacity of 96 mAh g^{-1} at 1 A g^{-1} from CP tests than MnO$_2$ (47 mAh g^{-1}). The first-order derivatives of CP (dQ/dv) plots were further analyzed to reveal the cathodic and anodic peaks, shown in Figure S4. The plots showed that (Ni)MnO$_2$ had two oxidation peaks (~ 0.4 V and 0.8 V) and two reduction peaks (~ 0.0 V and 0.7 V). Similar redox features were displayed in MnO$_2$ materials with more significant peak-broadening and slightly shifted peak positions, possibly due to the lower redox activity of MnO$_2$ and its more significant capacitive charge storage mechanism.

To further understand the electro-kinetics of (Ni)MnO$_2$ and MnO$_2$ birnessite, we analyzed the current (i) at different scan rates (v) at a given potential. Assuming the peak current (i) obeys the power-law relationship with the scan rate (v) at peak potential, and can be expressed as a combination of surface-controlled capacitive Na-ion storage (i$_1$ = a$_1$v) and diffusion-controlled Na-ion intercalation (i$_2$ = a$_2$v^{½}):

$i = a_1v + a_2v^{½} \approx av^b$

By fitting the value of b, insight into the Na-ion storage process can be provided. **Figure S5** shows the results for fitting the *b*-value of the peaks in all the anodic and cathodic scans. During anodic scans, the (Ni)MnO$_2$ showed the *b*-values of 0.75 and 0.9 for the two anodic peaks, higher than the *b*-values from MnO$_2$ (0.72 and 0.82). Similarly, the (Ni)MnO$_2$ showed a higher *b*-value of 0.82 for the major cathodic peak than MnO$_2$ (0.74). All the calculated *b*-values are between 0.5 and 1.0, suggesting both the surface-controlled capacitive and diffusion-limited redox processes contribute to the Na-ion storage in both

materials. However, (Ni)MnO$_2$ showed the larger *b*-values in each redox peak than MnO$_2$, suggesting a more capacitive charge storage process.

Electrochemical stability measurements of MnO$_2$ and (Ni)MnO$_2$ were conducted at 2 A g^{-1} for 100 charge and discharge cycles (**Figure S5**), and **Figure 1f** shows the discharge capacity retention. (Ni)MnO$_2$ showed better capacity retention after 100 cycles relative to MnO$_2$, demonstrating its electrochemical stability with less degradation due to Ni doping. Unlike (Ni)MnO$_2$, MnO$_2$ birnessite showed increasing capacities in the first five cycles and a typical capacity decay in the rest cycles. Although the exact mechanism of this conditioning process is still unknown, it is possibly due to the relatively large grain size of MnO$_2$ that might retard the contact between the electrode and electrolytes during the initial cycling. We have also collected several reported references in **Table S3**, demonstrating the comparable performance of our (Ni)MnO$_2$ relative to other MnO$_2$ with or without doing in terms of their charge storage capacity and cycling stability

The XAS measurement also confirmed the redox-active nature of Mn and Ni components. **Figure 2** shows Mn and Ni K-edge XAS spectra obtained from MnO$_2$ and (Ni)MnO$_2$ at a pristine state and a highly charged state of 1.25 V. The Mn spectra in both pristine MnO$_2$ and (Ni)MnO$_2$ materials exhibit a broad absorption maximum at 6559 eV and a pre-edge around 6541 eV. Although differences among the sample and reference edge shapes do not allow definite determination of oxidation states, the line shapes point at a valence state of Mn (IV). At a highly charged state of 1.25 V, the energy positions of 0.5μ(E) for Mn K-edge in both materials shift to the higher energy position relative to pristine materials, indicating the oxidation of Mn (**Figure 2a**). These findings agree with previous studies on lithium NCM-type transition metal oxides.[16] The nickel spectrum exhibits a broad absorption maximum at 8350 eV, corresponding to the allowable 1s→4p dipole transition. The subtle pre-edge feature at 8330 eV corresponds to a dipole transition from 1s to 3d/4p dipole, which is in fact formally forbidden and only allowable in distorted Ni-O octahedral.[4, 17]
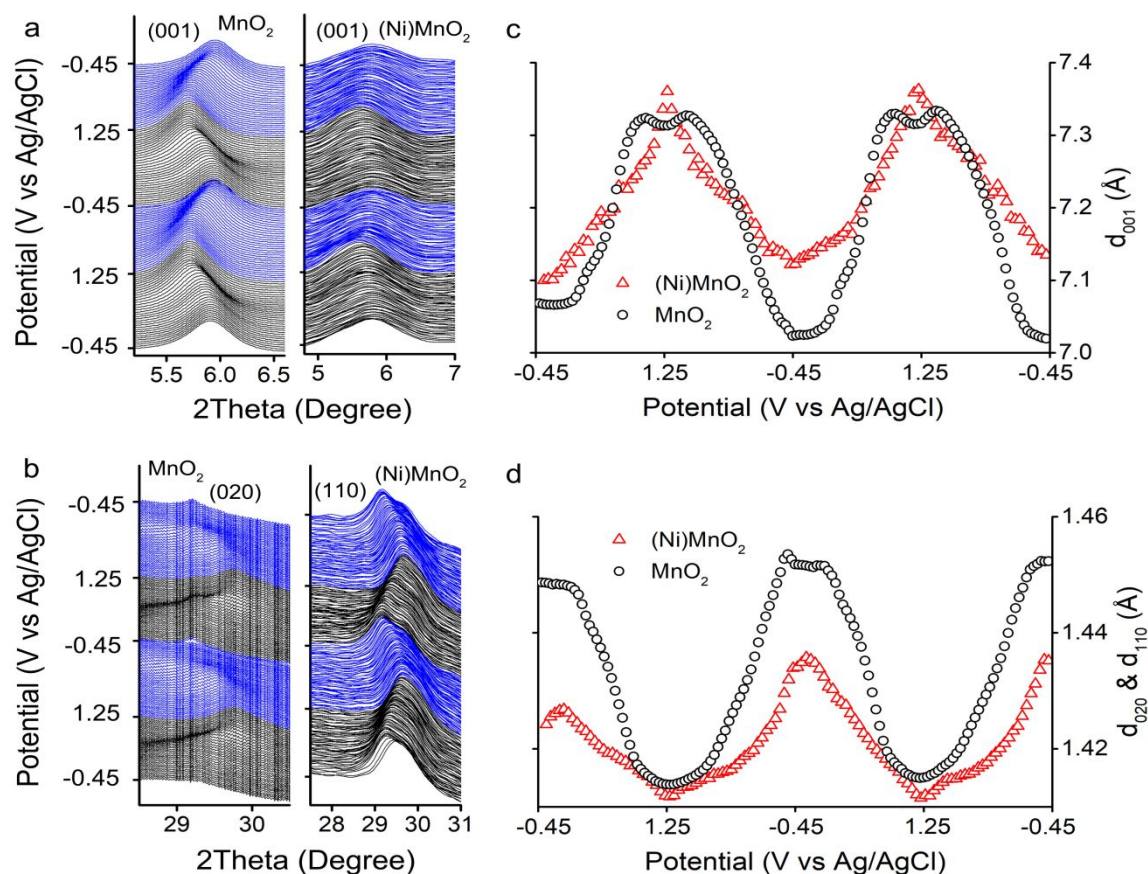
Figure 3. *In situ* XRD measurements of layered MnO_2 and $(Ni)MnO_2$. (a) The variations of layered peak (001) and (b) characteristic Bragg peaks (020) and (110) of MnO_2 and $(Ni)MnO_2$ during two CV scans; (c, d) the variations of layered spacing of d_{001} and Bragg plane distance d_{020} and d_{110} for MnO_2 and $(Ni)MnO_2$.

The pre-edge feature in Ni K-edge data is congruent with the disordered nature of Ni-site, obtained from the PDF analysis. The energy positions of $0.5\mu(E)$ increased slightly from 8340.5 eV to 8340.8 eV from pristine to the deep charged state, indicative of an oxidized Ni valence upon charging (**Figure 2b**). The pristine $(Ni)MnO_2$ showed Ni-K edge is closed to $LiNiO_2$ and suggested a valence state of Ni^{3+}, which evolves to $Ni^{3+/4+}$ when charged to 1.25 V. Collectively, the XAS results provide clear evidence of the contribution of Mn and Ni to the redox activities during electrochemical cycling. Notably, the Ni-induced charge reduction on lattice oxygen was partially validated by the XAS results shown in **Figure 2**. At the highly charged states (1.25V), Mn- and Ni-ion valence were close to 4+. As a result, mixing metal-oxygen band (*d-p* mixing) between oxygen 2p orbitals and the partial electron filled Ni 3d e_g orbital could form $Ni^{3+/4+}$-O^{2-} configuration. Such Ni-O covalency leads to depletion of negative charge from oxygen atom to nickel.[4, 5] While for the Mn atoms, negative charge transfer from lattice oxygen occurs in a relatively less distinct manner since its oxidation state continuously increases to even above 4+, indicating the Mn^{4+}-O bond is more ionic and less covalent compared to that of Ni^{4+}-O interaction.[16]

To further illustrate valence states of Mn in the $(Ni)MnO_2$ electrode materials, *ex-situ* X-ray photoelectron spectroscopy (XPS) analysis was carried out to study Mn spectra of the fully discharged (at -0.45 V vs. Ag/AgCl) and charged (at 1.25 V vs. Ag/AgCl) $(Ni)MnO_2$, as shown in **Figure S7**. Notably, the Mn 3s peak has two major multiplet split components due to the coupling between non-ionized 3s electrons with 3d valence-band electrons. Thus, splitting magnitude relates to the oxidation state of Mn, where smaller peak splitting (ΔE) means a higher valence state. **Figure S7** shows that charged $(Ni)MnO_2$ electrode had the smallest ΔE (4.34 eV) of Mn multiplet split in Mn 3s spectra than discharged (4.83 eV) and pristine (4.66 eV) materials, and even smaller than MnO_2 standard (4.70 eV).[18] Thus, the XPS data suggest the Mn components in full charged $(Ni)MnO_2$ electrode materials appear more oxidized valence state, congruent with XAS measurements.

In situ XRD measurements were performed on MnO_2 and $(Ni)MnO_2$ during the charge/discharge processes, where two consecutive CV scans were performed under a potential window between -0.45 V and 1.25 V (vs. Ag/AgCl). **Figures 3a and 3b** show the evolution of crystal structures as a function of potential, especially the variations of (001) basal peaks and characteristic (020) and (110) Bragg peaks. The corresponding d-spacing of the above peaks are plotted in **Figures 3c and 3d**. The (001) peaks of birnessite shifted to a lower 2θ angle with the increasing d_{001} values during the oxidation process and *vice versa* upon the reduction process. Increasing d_{001} values during the charging (oxidation) process are attributed to the increased

electrostatic repulsion between Mn-O octahedral upon the Na-ion removal from the interlayer region. On the other hand, (020) or (110) Bragg peaks show an opposite trend compared to (001) basal diffraction peaks. During the oxidation process, the Na-ion removal from the interlayer region leads to continuous oxidization of Mn- and Ni-ions with decreasing ionic radii, and thus d_{020} and d_{110} decrease. On average, MnO_2 goes through about 4.2% variation of the (001) interlayer distance during the whole redox process, larger than that of $(Ni)MnO_2$ (3.2%).

Table 1. The listed layered and Bragg plane distance at certain potentials during 2nd CV scan for MnO_2 and $(Ni)MnO_2$. (Note: the maximum c-lattice is shaded in grey)

Potential (V)		MnO_2		$(Ni)MnO_2$	
		$d_{(001)}$	$d_{(020)}$	$d_{(001)}$	$d_{(110)}$
Anodic Scan ↓ *Cathodic Scan*	-0.45	7.023	1.452	7.124	1.435
	0.95	7.330	1.417	7.285	1.416
	1.25	7.315	1.415	7.362	1.411
	1.05	7.334	1.416	7.305	1.414
	-0.45	7.019	1.452	7.134	1.435

Though MnO_2 and $(Ni)MnO_2$ share similar structural evolutions in general during charge/discharge processes, they showed different trends in c-lattice evolution at the deep charging process when potential increased from ~1.0 V to 1.25 V (**Table 1**). During early-stage charging as the potential increases from -0.45 V to 0.95 V, MnO_2 undergoes an expected increase of d_{001} (7.023 Å to 7.330 Å). But as potential further increases from 0.95 V to 1.25 V, unexpected c-lattice collapses occur (7.330 Å to 7.315 Å). On the subsequent reduction process, MnO_2 shows an expansion of (001) spacing from 7.315 Å to 7.334 Å as the potential decreases from 1.25 V to 1.05 V, followed by shrinkage of d_{001} from 7.334 Å to 7.019 Å when the potential further decreases to -0.45 V. The shrinkage of d_{001} in MnO_2 at the deep charge accounting for 0.2% variation in c-lattice. In stark contrast, $(Ni)MnO_2$ birnessite exempts from the lattice collapse at deep charging even the $(Ni)MnO_2$ appears higher charge and discharge capacity than MnO_2. When the potential increases from -0.45 V to 1.25 V, $(Ni)MnO_2$ shows a continuous increase of d_{001} from 7.124 Å to 7.362 Å, followed by a decreasing d_{001} from 7.362 Å to 7.134 Å throughout the entire discharge process. Notably, d_{020} and d_{110} of MnO_2 and $(Ni)MnO_2$ continuously decrease throughout the entire oxidation process, showing from 1.452 Å to 1.415 Å (d_{020}) and from 1.453 Å to 1.411 Å (d_{110}), confirming both Mn and Ni undergo an oxidation process during the entire charging process and *vice versa* during the discharging process.

Typically, cations residing between interlayers (e.g., Li^+, Na^+) diminish the electrostatic repulsion between negatively charged lattice oxygen from adjacent metal-oxygen slabs. However, transitional metals (e.g., Mn, Co, Ni) further oxidizes close to 4+ at deep charge state, their 3d and O 2p orbitals are highly hybridized. The resulting negative charge depletion from lattice oxygen decreases O effective charge. Therefore, c-lattice collapses because of much-reduced inter-slab repulsion, though it also depends on the chemical compositions. For instance, Ni-rich NCM811 cathode has the c-lattice decrease from the maximum 14.467 Å to 14.030 Å (~ 3.0% variation), while NCM111 cathode only experiences collapses from 14.500 Å to 14.480 Å (0.1%) during delithiation.[4, 5] The increased Ni portion
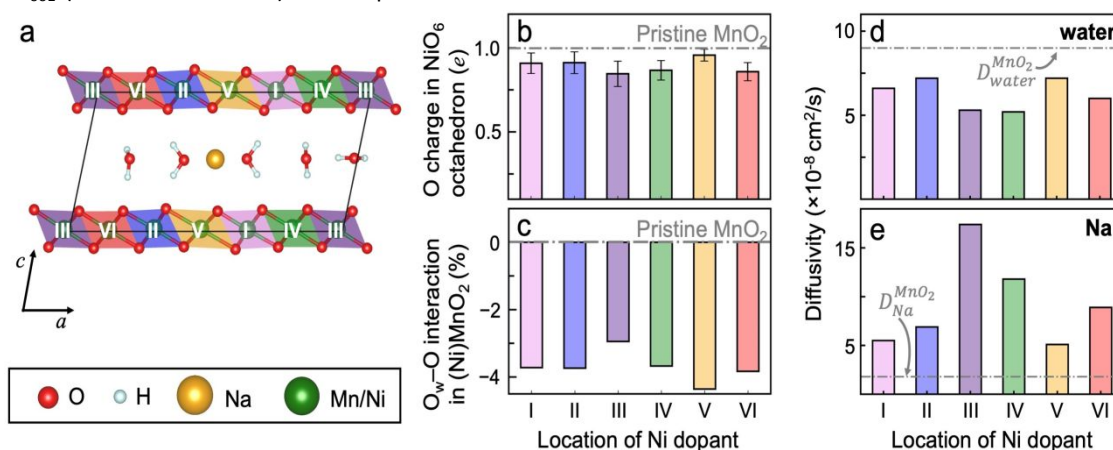
Figure 4. Atomic-scale simulations to understand interactions between lattice oxygen and structural water in $(Ni)MnO_2$ under deep charge conditions. (a) Equilibrium atomic configuration of pristine Na-birnessite under Na-lean conditions (deep charge) with composition $Na_{0.17}MnO_2 \cdot 0.833H_2O$ obtained from total energy DFT calculations. The six distinct possible sites for substituting Mn with Ni dopants are marked as I-VI. Mn atoms at each of these sites are individually replaced with a Ni-atom to obtain $Na_{0.17}Ni_{0.17}Mn_{0.83}O_2 \cdot 0.833H_2O$. (b) Bader charge on the O atoms belonging to the NiO_6 octahedron for different locations of Ni dopant, and (c) Percentage change in the electrostatic repulsion between the oxygen atoms belonging to lattice (O) and structural water (O_w) in $Ni(Mn)O_2$ as compared to that in pristine MnO_2 for different location of Ni-dopant. The average charge on O atoms surrounding MnO_6 octahedra (panel (b)) in pristine MnO_2 is shown by gray line for comparison. Room temperature diffusivity of (d) structural water, and (e) Na^+ ion in $Na_{0.17}Ni_{0.17}Mn_{0.83}O_2 \cdot 0.833H_2O$ for different locations of Ni dopant obtained from classical molecular dynamics simulations. In panels (d) and (e), room temperature diffusivity of structural water ($D_{water}^{MnO_2} = 9 \times 10^{-8}$ cm²/s) and Na^+ ion ($D_{Na}^{MnO_2} = 1.8 \times 10^{-8}$ cm²/s), respectively, in pristine MnO_2 are indicated by gray line for comparison.
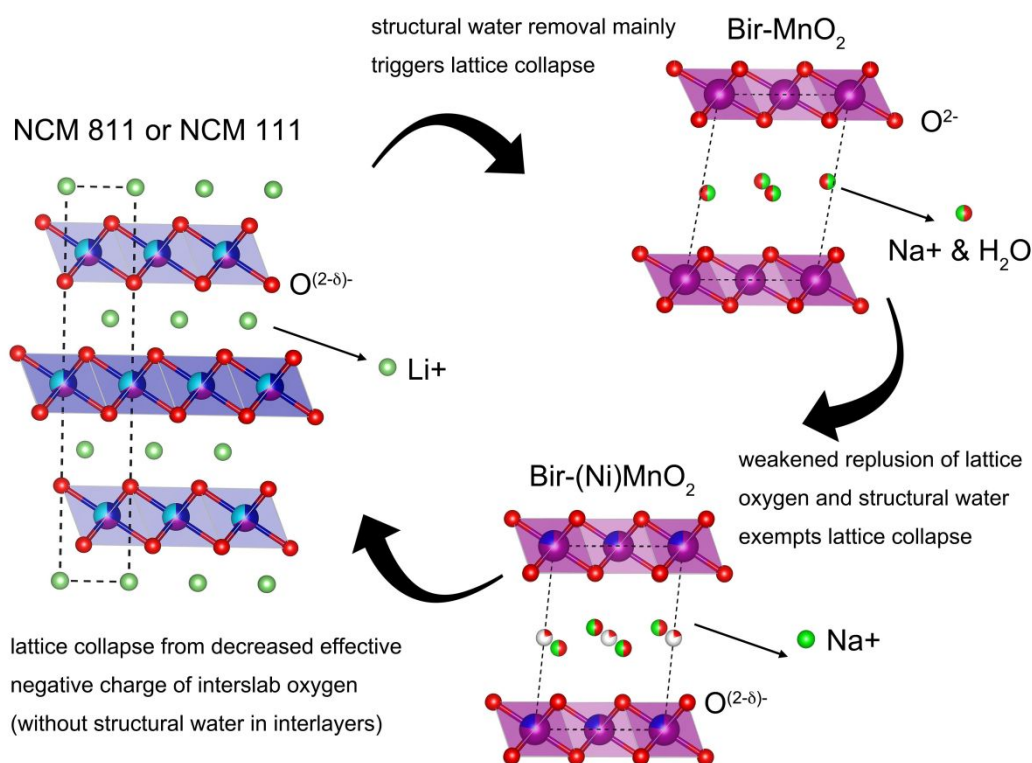
Figure 5. Mechanisms of *c*-lattice collapse for the NCM, Bir-MnO$_2$ and Bir-(Ni)MnO$_2$ cathodes at high voltage (Mn: magenta, Ni: blue, Co: Cyan, O: red, Na: green, Li: light green, Note: the interlayer red atoms are from structural water molecules and O$^{(2-\delta)-}$ indicates the decreased oxygen electronegativity).

in NCM shows a more distinct lattice collapse, probably due to a more strongly Ni-O mixed band than Co-O and Mn-O. Notably, the above lattice collapse mechanism, well recognized in non-aqueous Li intercalated NCM electrode materials, is distinguishable for our reported aqueous birnessite-type MnO$_2$ materials. Generally speaking, Mn-O mixed band is less covalent relative to Ni-O one, and less charge depletion on oxygen is expected and would strengthen inter-slab repulsion (and would prevent *c*-lattice collapse). Therefore, we may not expect to observe too much lattice collapse for MnO$_2$ at high voltage or just very minimum (smaller than 0.1%). On the contrary, MnO$_2$ shows a 0.2% *c*-lattice collapse at the deep charge state, more prominent than non-aqueous NCM111 materials. This unusual lattice collapse observed in MnO$_2$ birnessite is likely attributed to structural water removal accompanied by a de-sodiation process at high voltage (1.25 V). Specifically, the "pillar" effect of structural water in the interlayer space was alleviated after the extraction of highly hydrated Na-ion, causing *c*-lattices contraction.

Interestingly, with Ni doping into birnessite MnO$_2$, no *c*-lattice collapse is observed for (Ni)MnO$_2$ at high voltage even though Ni-O covalency could potentially increase its ability to reduce inters-lab repulsion, different from non-aqueous NCM 811 and NCM 111 materials. We then employ density functional theory (DFT) calculations [19-23](See Supplementary Information for details of the calculations) to elucidate the atomic interaction between lattice oxygen (constituting MnO$_6$ or NiO$_6$ octahedra) and structural water molecules in Ni-doped

birnessite under the deep charge conditions (**Figure 4**). Similar to our experiments and previous DFT reports, we find that (Ni)MnO$_2$ birnessite exhibits a monoclinic crystal structure with an interlayer spacing of d_{001} ranges between 7.14 Å to 8.75 Å, depending on the extent of hydration (0.75 H$_2$O/MnO$_2$ to 1.5 H$_2$O/MnO$_2$).[24, 25] Importantly, replacing Mn atom with Ni is energetically uphill by only ~0.18 eV/atom irrespective of the location of Ni dopant; the interlayer distances of Ni-doped birnessite are within ~0.1 Å of the undoped counterpart (**Figure 4a**, **Table S4**). In MnO$_2$ birnessite, the mean Bader charge on the lattice oxygen forming MnO$_6$ octahedra is –0.99e. **Figure 4b** shows that replacing Mn with Ni yields a lower charge. **Figure 4b** shows that replacing Mn with Ni yields a lower charge on lattice oxygens surrounding Ni, irrespective of the location of the Ni dopant. This lowering of charge on lattice oxygens can be attributed to the high electronegativity of Ni as compared to Mn (Ni: 1.91 vs. Mn: 1.55 on the Pauling scale). The extent of charge reduction on lattice oxygen depends on the location of Ni dopant, ranging from –0.85e at Site VI to –0.95e at Site V, primarily due to differences in separation distance between Ni-dopant and intercalating Na-ion. For Ni locations that are close to Na-ion (e.g., Site V), the extremely low electronegativity of Na (0.93) allows minimal change in charge of neighboring lattice oxygen (i.e., O belonging to NiO$_6$). In contrast, when Ni dopant is sufficiently far away from Na-ion (e.g., Site VI), the electronegativity difference between Mn and Ni causes a significant reduction of charge on lattice oxygen of NiO$_6$. Nevertheless, the reduced charge on lattice oxygen (induced by

Ni-doping) results in lower total electrostatic repulsion between lattice oxygen (O) and structural water oxygen (O_w) in (Ni)MnO$_2$ as compared to that in MnO$_2$ birnessite (**Figure 4c**), with the reduction in O_w-O interaction ranging from 2.94% at site III to 4.35% at site V. Note that the reduced O_w-O electrostatic interactions do not yield significant contraction along *c*-axis (**Table S3**). This is mainly because the Ni-induced reduction in charge on lattice oxygen lowers both the repulsive O_w-O, and attractive Na-O_w electrostatic interactions (as compared to that in pristine birnessite MnO$_2$) . The two effects largely cancel each other out, causing minimal impact on interlayer spacing in (Ni)MnO$_2$.

Direct visualization of equilibrium configurations of (Ni)MnO$_2$ provide further insights into the impact of O_w-O interactions on the solvation structure around intercalating Na$^+$ cation. Na$^+$ ions prefer to coordinate with anionic oxygen atoms belonging to structural water (O_w) or Ni/Mn-centered O-octahedra. In MnO$_2$ birnessite, Na$^+$ is surrounded by 6 water molecules (with one O_w from each water within 2.29 Å from Na$^+$) and 2 lattice oxygens (with Na-O distance of ~2.66 Å). Previous investigations have also reported similar nearest-neighbor Na-O_w distances on Na$^+$ solvation in water.[26] Upon introducing Ni to any site I-VI, reduction in O_w-O electrostatic repulsion causes O_w from one of the solvating water to move closer to the lattice oxygens (closest O-Ow distance is < 2.6 Å), forming a new hydrogen bond. Meanwhile, this water molecule leaves the solvation shell surrounding Na$^+$ (Na-O_w distance > 3.5 Å) for all Ni locations.

To investigate the effect of Ni-induced reduction in electrostatic O_w-O interactions on the mobility of structural water and Na$^+$ ions, we turn to classical molecular dynamics (CMD) simulations using a well-established ClayFF interatomic potential (See Supporting Information for details of the simulations). We employed the atomic charges obtained from our DFT calculations to account for electrostatic interactions accurately. Notably, previous CMD studies have shown that this approach provides an excellent description of the structure, thermodynamics, ion-solvation behavior, and transport properties of MnO$_2$ birnessite. Our CMD simulations show that the diffusivity of structural water in pristine MnO$_2$ birnessite $D^{MnO_2}_{water}$ (9×10^{-8} cm^2/s) is nearly 4 orders of magnitude slower than that in bulk liquid water, consistent with previous reports. Upon Ni-doping, we find that the reduced O_w-O electrostatic repulsive interactions cause significant lowering of diffusivity of structural water (20%–42%, depending on the location of Ni-dopant) compared to that in pristine MnO$_2$ (**Figure 4d**). The differences in diffusivity of structural water in (Ni)MnO$_2$ arise from the variation in charge on lattice oxygen owing to the location of Ni-dopant (**Figure 4b**). We also observe a concurrent increase in the diffusivity of intercalating Na$^+$ ions with Ni-doping (**Figure 4e**). Evidently, Ni-doping facilitates immobilization of structural water as compared to pure MnO$_2$ birnessite.

Conclusions

The layered type of manganese oxides, including birnessite MnO$_2$ and (Ni)MnO$_2$ are synthesized and also characterized by X-ray diffraction and X-ray PDF analysis. *In situ* XRD shows abnormal shrinkage and expansion of layered lattice at the high voltage only occurs in the MnO$_2$ layered birnessite while not for (Ni)MnO$_2$. DFT calculations indicate that the higher electronegativity of Ni-dopant (compared to Mn) facilitates lowering of charge on lattice oxygen, which in turn, reduces the repulsive O_w-O interactions. CMD simulations using atomic charges derived from DFT confirm that Ni-induced reduction of charge on lattice oxygen enables immobilization of structural water as compared to pristine MnO$_2$ birnessite. *Ex situ* XANES points out, though there is decreased electronegativity of oxygen atoms from Ni-O covalency since Ni(IV) forms at high voltage, such differences in lattice variation mechanism is not simply from Ni-O effect, and it is more likely that the decreased repulsion force between lattice oxygen and structural water oxygen results in smaller mobility of structural water in (Ni)MnO$_2$ birnessite relative to MnO$_2$ and then exempts (Ni)MnO$_2$ from *c*-lattice collapse (**Figure 5**). Unlike Li-metal oxides, where lattice oxygen repulsions determine the interlayer distance between adjacent metal-oxygen molecular layers, our data collectively demonstrated that decreased repulsion between lattice oxygen and structural water oxygen (Ni)MnO$_2$ decreased structural water mobility and thus prohibited the removal of water molecule along with Na-ions during high-voltage charging, preventing the *c*-lattice from shrinkage at highly charged state. This new understanding of the interplay between lattice oxygen and water molecule will guide designing the layered electrodes with a high capacity and stability for energy storage.

Author Contributions

X.T. and X.S. conceived the research idea and designed the experiments. X.S. contributed to material synthesis and material characterizations. X.S. contributed to the electrochemical experimental measurements. X.S., S.K., W.X., M.A., G.K. and D.O. contributed to in situ X-ray measurements. X.S. and X.T. contributed to ex situ XAS measurements. X.S. contributed to the X-ray analysis. R.P. and B.N. designed the atomic-scale calculations. R.P. performed all the atomic-scale simulations under guidance of B.N.. X.S. and X.T. wrote the manuscript with contribution from R.P. and B.N. X.T. supervised the project. All authors discussed the results and commented on the manuscript.

Conflicts of interest

There are no conflicts to declare.

Acknowledgements

Notes and references

1. M. D. Radin, S. Hy, M. Sina, C. Fang, H. Liu, J. Vinckeviciute, M. Zhang, M. S. Whittingham, Y. S. Meng and A. Van der Ven, *Advanced Energy Materials*, 2017, **7**, 1602888.
2. J. Xu, F. Lin, M. M. Doeff and W. Tong, *Journal of Materials Chemistry A*, 2017, **5**, 874-901.
3. M. Bianchini, M. Roca-Ayats, P. Hartmann, T. Brezesinski and J. Janek, *Angewandte Chemie International Edition*, 2019, **58**, 10434-10458.
4. A. O. Kondrakov, H. Geßwein, K. Galdina, L. de Biasi, V. Meded, E. O. Filatova, G. Schumacher, W. Wenzel, P. Hartmann, T. Brezesinski and J. Janek, *The Journal of Physical Chemistry C*, 2017, **121**, 24381-24388.
5. A. O. Kondrakov, A. Schmidt, J. Xu, H. Geßwein, R. Mönig, P. Hartmann, H. Sommer, T. Brezesinski and J. Janek, *The Journal of Physical Chemistry C*, 2017, **121**, 3286-3294.
6. N. Zhang, M. Jia, Y. Dong, Y. Wang, J. Xu, Y. Liu, L. Jiao and F. Cheng, *Advanced Functional Materials*, 2019, **29**, 1807331.
7. H. Li, A. Liu, N. Zhang, Y. Wang, S. Yin, H. Wu and J. R. Dahn, *Chemistry of Materials*, 2019, **31**, 7574-7583.
8. Q. Liu, X. Su, D. Lei, Y. Qin, J. Wen, F. Guo, Y. A. Wu, Y. Rong, R. Kou, X. Xiao, F. Aguesse, J. Bareño, Y. Ren, W. Lu and Y. Li, *Nature Energy*, 2018, **3**, 936-943.
9. X. Shan, F. Guo, D. S. Charles, Z. Lebens-Higgins, S. Abdel Razek, J. Wu, W. Xu, W. Yang, K. L. Page, J. C. Neuefeind, M. Feygenson, L. F. J. Piper and X. Teng, *Nature Communications*, 2019, **10**, 4975.
10. L. Athouël, F. Moser, R. Dugas, O. Crosnier, D. Bélanger and T. Brousse, *The Journal of Physical Chemistry C*, 2008, **112**, 7270-7277.
11. Q. Xie, W. Li and A. Manthiram, *Chemistry of Materials*, 2019, **31**, 938-946.
12. K. Wang, H. Wan, P. Yan, X. Chen, J. Fu, Z. Liu, H. Deng, F. Gao and M. Sui, *Advanced Materials*, 2019, **31**, 1904816.
13. W. Li, X. Liu, H. Celio, P. Smith, A. Dolocan, M. Chi and A. Manthiram, *Advanced Energy Materials*, 2018, **8**, 1703154.
14. M. Yeager, W. X. Du, R. Si, D. Su, N. Marinkovic and X. W. Teng, *J. Phys. Chem. C*, 2012, **116**, 20173-20181.
15. X. Shan, F. Guo, K. Page, J. C. Neuefeind, B. Ravel, A. M. M. Abeykoon, G. Kwon, D. Olds, D. Su and X. Teng, *Chemistry of Materials*, 2019, **31**, 8774-8786.
16. K. Luo, M. R. Roberts, R. Hao, N. Guerrini, D. M. Pickup, Y.-S. Liu, K. Edström, J. Guo, A. V. Chadwick, L. C. Duda and P. G. Bruce, *Nature Chemistry*, 2016, **8**, 684-691.
17. Y. W. Tsai, B. J. Hwang, G. Ceder, H. S. Sheu, D. G. Liu and J. F. Lee, *Chemistry of Materials*, 2005, **17**, 3191-3199.
18. M. C. Biesinger, B. P. Payne, A. P. Grosvenor, L. W. M. Lau, A. R. Gerson and R. S. C. Smart, *Applied Surface Science*, 2011, **257**, 2717-2730.
19. G. Kresse and J. Furthmüller, *Physical Review B*, 1996, **54**, 11169-11186.
20. G. Kresse and D. Joubert, *Physical Review B*, 1999, **59**, 1758-1775.
21. J. P. Perdew, K. Burke and M. Ernzerhof, *Physical Review Letters*, 1996, **77**, 3865-3868.
22. A. I. Liechtenstein, V. I. Anisimov and J. Zaanen, *Physical Review B*, 1995, **52**, R5467-R5470.
23. D. A. Tompsett, S. C. Parker and M. S. Islam, *Journal of Materials Chemistry A*, 2014, **2**, 15509-15518.
24. W. Cheng, J. Lindholm, M. Holmboe, N. T. Luong, A. Shchukarev, E. S. Ilton, K. Hanna and J.-F. Boily, *Langmuir*, 2021, **37**, 666-674.
25. K. P. Lucht and J. L. Mendoza-Cortes, *The Journal of Physical Chemistry C*, 2015, **119**, 22838-22846.
26. A. C. Belch, M. Berkowitz and J. A. McCammon, *Journal of the American Chemical Society*, 1986, **108**, 1755-1761.